



RESEARCH ARTICLE

10.1029/2022JA030749

Decadal and Annual Variations in Meteoric Flux From Ulysses, Wind, and SOFIE Observations

Mark E. Hervig¹ , David Malaspina^{2,3} , Veerle Sterken⁴ , Lynn B. Wilson III⁵ ,
Silvan Hunziker⁴, and Scott M. Bailey⁶ 

¹GATS, Driggs, ID, USA, ²Laboratory for Atmospheric and Space Physics, University of Colorado, Boulder, CO, USA,

³Astrophysical and Planetary Sciences Department, University of Colorado, Boulder, CO, USA, ⁴Institute for Particle Physics and Astrophysics, Swiss Federal Institute of Technology, Zürich, Switzerland, ⁵NASA Goddard Spaceflight Center, Greenbelt, MD, USA, ⁶Virginia Polytechnic Institute, Blacksburg, VA, USA

Key Points:

- Solar Occultation For Ice Experiment, Wind, and Ulysses give consistent estimates of the meteoric influx at Earth
- Annual and decadal variations in Wind interstellar dust observations agree with model simulations
- Both interstellar and interplanetary dust are correlated to the 22-year solar magnetic cycle

Correspondence to:

M. E. Hervig,
m.e.hervig@gats-inc.com

Citation:

Hervig, M. E., Malaspina, D., Sterken, V., Wilson, L. B. III, Hunziker, S., & Bailey, S. M. (2022). Decadal and annual variations in meteoric flux from Ulysses, Wind, and SOFIE observations. *Journal of Geophysical Research: Space Physics*, 127, e2022JA030749. <https://doi.org/10.1029/2022JA030749>

Received 14 JUN 2022
Accepted 30 SEP 2022

Abstract Our solar system is filled with meteoric particles, or cosmic dust, which is either interplanetary or interstellar in origin. Interstellar dust (ISD) enters the heliosphere due to the relative motion of the sun and the interstellar flow. Interplanetary dust (IPD) comes primarily from asteroid collisions or comet sublimation, and comprises the bulk of material entering Earth's atmosphere. This study examines variations in ISD and the IPD flux at Earth using observations from three different satellite techniques. First are size-resolved in situ meteoroid detections by the Ulysses spacecraft, and second are in situ indirect dust observations by Wind. Third are measurements of meteoric smoke in the mesosphere by the Solar Occultation For Ice Experiment (SOFIE). Wind and Ulysses observations are sorted into the interstellar and interplanetary components. Wind ISD show the anticipated correlation to the 22-year solar magnetic cycle, and are consistent with model predictions of ISD. Because Wind does not discriminate particle size, the IPD measurements were interpreted using meteoric mass distributions from Ulysses observations and from different models. Wind observations during 2007–2020 indicate a total meteoric influx at Earth of 22 metric tons per day ($t\ d^{-1}$), in reasonable agreement with long-term averages from SOFIE ($25\ t\ d^{-1}$) and Ulysses ($32\ t\ d^{-1}$). The SOFIE and Wind influx time series both show an unexpected correlation to the 22-year solar cycle. This relationship could be an artifact, or may indicate that IPD responds to changes in the solar magnetic field.

1. Introduction

The solar system is filled with meteoric particles, or cosmic dust, which is interplanetary or interstellar in origin. Interplanetary dust (IPD) comes primarily from asteroid collisions or comet sublimation, and is typically bound to solar orbits on the ecliptic plane. Interstellar dust (ISD) enters the heliosphere due to the relative motion of the sun within the local interstellar cloud (Krüger et al., 2019; Sterken et al., 2019). Meteoroids are constantly entering Earth's atmosphere, with larger IPD particles (roughly 1–100 μm radius) dominating the mass influx. Frictional heating during entry vaporizes a fraction of the particles at altitudes from ~ 80 to 100 km, and the ablation products combine to form nanometer sized meteoric smoke particles that reside in the mesosphere and stratosphere (Hervig et al., 2017; Plane, 2012). Smoke in the mesosphere is reduced during polar summer due to transport by the mesospheric meridional circulation, as indicated by models (Bardeen et al., 2008; Megner et al., 2008) and satellite observations (Hervig et al., 2009). The annual smoke variation occurs despite the seasonal change in meteor influx at polar latitudes, where the highest influx occurs in summer as shown by radars (Janchez et al., 2004; Reid et al., 2006; Singer et al., 2004). A comprehensive assessment of the spatial and temporal dependence in meteoric influx can be found in Fentzke et al. (2009). Recent estimates of the meteoric influx into Earth's atmosphere are from ~ 15 to 60 metric tons per day ($t\ d^{-1}$) (e.g., Carrillo-Sánchez et al., 2020), an improvement over the bewildering range of previous decades (1–300 $t\ d^{-1}$) (e.g., Plane, 2012). The meteoric influx at Earth has implications for atmospheric chemistry, aerosol processes, and ocean productivity (e.g., Rudraswami et al., 2021), motivating further improvements to the understanding of influx and its variability.

The present study examines meteoric flux in the near-Earth environment using observations from Ulysses, Wind, and the Solar Occultation For Ice Experiment (SOFIE). The Wind and Ulysses spacecraft offer long-term records of in situ dust measurements, which are related here to meteoric smoke measurements from the SOFIE satellite instrument. Interpreting the Ulysses, Wind, and SOFIE measurements requires an understanding of the meteoric mass distribution, and dust enhancement due to Earth's gravity and size. The Ulysses and Wind

© 2022. The Authors.

This is an open access article under the terms of the [Creative Commons Attribution License](https://creativecommons.org/licenses/by/4.0/), which permits use, distribution and reproduction in any medium, provided the original work is properly cited.

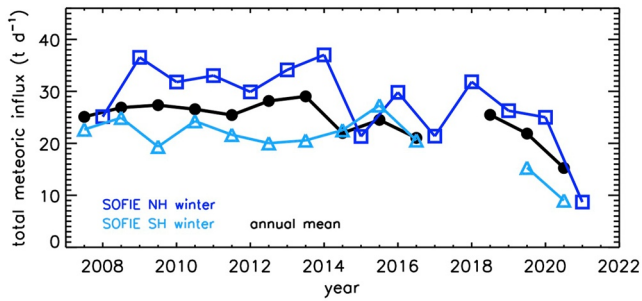


Figure 1. Time series of Solar Occultation For Ice Experiment (SOFIE) total meteoric influx into Earth's atmosphere from measurements in the Northern and Southern Hemispheres during winter months (November–February in the NH and May–August in the SH). The annual mean for both hemispheres is also shown.

observations contain both IPD and ISD, and separating these is important for estimating the meteoric influx at Earth. The Wind ISD results are validated through comparisons with ISD simulations from the Interplanetary Meteoroid environment for EXploration (IMEX) model (Sterken et al., 2015; Strub et al., 2019).

2. SOFIE Observations

SOFIE has conducted solar occultation measurements from the Aeronomy of Ice in the Mesosphere (AIM) satellite since 2007 (Russell et al., 2009). The measurements are used to retrieve vertical profiles of temperature, five gases (O_3 , H_2O , CO_2 , CH_4 , and NO), polar mesospheric cloud (PMC) extinction at 11 wavelengths, and meteoric smoke extinction at three wavelengths (330, 867, and 1037 nm). SOFIE observes primarily polar latitudes, with the exception of 2017–2019 when orbital progression caused an excursion through the tropics and a change from sunsets in the Southern Hemisphere (SH) to the Northern Hemisphere (NH) (vice versa for sunrises, see Hervig et al., 2021 for details). The current SOFIE data is version 1.3 which is available online (sofie.gats-inc.com).

SOFIE measurements have been used to characterize the variation of smoke in height and time, and revealed the chemical composition of smoke (Hervig et al., 2009, 2017). The smoke extinctions used here are monthly zonal means, avoiding summer measurements when PMCs contaminate the smoke signal (Hervig et al., 2012). Extinction is converted to volume density for a smoke composition of olivine ($Mg_{2x}Fe_{2-2x}SiO_4$, $x = 0.4$), which is optically detected by SOFIE. Volume density is then used to derive the ablated meteoric influx through comparisons with smoke simulations from the Whole Atmosphere Community Climate Model (WACCM) (Bardeen et al., 2008; Hervig et al., 2017, 2021). SOFIE results during 2007–2020 indicate a global mean ablated influx into Earth's atmosphere of 7 ± 2 metric tons per day ($t d^{-1}$). Since only $\sim 30\%$ of incoming meteoroids are ablated (Carrillo-Sánchez et al., 2020), the corresponding total influx (ablated plus surviving material) is $25 \pm 7 t d^{-1}$. The influx versus time from SOFIE observations is shown in Figure 1, where the results indicate year-to-year variations and greater influx in the NH than in the SH. The hemispheric difference is still not understood, but could indicate an asymmetry in meteoric influx that is not represented in WACCM. The results below consider the meteoric influx from SOFIE as the average of the NH and SH values.

3. Wind Observations

The Wind spacecraft was launched in 1994 to quantify the dynamics of the Sun-Earth system (Wilson et al., 2021). Wind operates within 1° of the ecliptic plane and has orbited the first Lagrange point (L1) since July 2004 ($\sim 1.5 \times 10^6$ km sunward from Earth). Prior to 2004, Wind conducted a variety of orbital maneuvers, including petal orbits through the magnetosphere, lunar flybys, and an excursion to the second Lagrange point (Malaspina & Wilson, 2016; Wilson et al., 2021). Many of these periods are not useful for dust measurements, and were screened from the analyses presented here.

Meteoroids are detected when they collide with Wind and a fraction of the spacecraft body is vaporized and ionized (Mann et al., 2019). The resulting plasma perturbs the electric potential of spacecraft surfaces (Shen et al., 2021), which is observed by the WAVES electric field antennas and recorded by the Time Domain Sampler (Bougeret et al., 1995). A similar approach has been used for dust measurements by other spacecraft including Voyager (Gurnett et al., 1983) and the Mars Atmosphere and Volatile Evolution Mission (Andersson et al., 2015). The Wind dust detector area is the cross-sectional area of the cylindrical spacecraft body (1.8 m height \times 2.4 m diameter), or $4.3 m^2$. Wind is estimated to be sensitive to meteoroids with radii (r) of 0.1–11 μm , or 10^{-14} to 10^{-8} g in mass (m) for a dust density of $\rho = 2.65 g cm^{-3}$, but cannot resolve the size of individual impactors. Malaspina et al. (2014) noted that the lower and upper mass bounds are uncertain by a factor of 10 or more, due to observational uncertainties and assumptions in the measurement interpretation. Wind reports the number of dust detections per day, which represents particles with m from 10^{-14} to 10^{-8} g. The Wind dust observations are discussed in detail by Malaspina et al. (2014), Meyer-Vernet et al. (2014), Kellogg et al. (2016), and

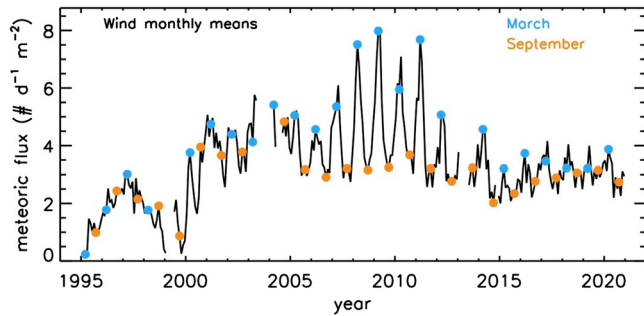


Figure 2. Time series of Wind meteoric flux, as the average during each month. Results for March and September are indicated.

Wood et al. (2015). Malaspina and Wilson (2016) describe the archived data which are available online (cdaweb.gsfc.nasa.gov). The Wind dust record is summarized in Figure 2, where the monthly average meteoric flux is shown. For this work, observations were ignored when there were known problems, or complications due to special spacecraft maneuvers (see Malaspina & Wilson, 2016; Wilson et al., 2021). The results indicate pronounced decadal and annual variations (e.g., more dust in March than September), which are investigated below.

4. Ulysses Observations

Ulysses operated during 1990–2007, and was the first spacecraft to conduct a polar orbit of the Sun. An in situ dust detector used impact ionization to measure the mass of individual particles with m from $\sim 10^{-16}$ – 10^{-6} g (Grün et al., 1992; Krüger et al., 2006, 2019). The detector sensitive area is quoted as a maximum of 0.02 m^2 by Krüger et al. (2015), which is the value used here. The Ulysses dust observations are illustrated in Figure 3a, where the mass and radius of each particle are shown. The reported particle mass uncertainties are typically a factor of 5–10, due to measurement errors combined with uncertainties in the interpretation. Due to the high-inclination polar orbit of the Sun, the Ulysses data set consists mostly of ISD. Strub et al. (2015) describe the criteria for identifying ISD in Ulysses, and the present study considered these (in reverse) to find IPD in the Ulysses record. Particles detected at high ecliptic latitudes (b, Figure 3b) are most likely interstellar in origin (Krüger et al., 2006), since interplanetary dust is concentrated near the ecliptic plane (e.g., Soja et al., 2019). Exceptions can occur, however, as dust from Halley type comets and Oort cloud comets has been detected far above the ecliptic plane. IPD in the near-Earth environment was identified by considering (a) spacecraft—sun distances (D_S) of less than 1.5 AU, and (b) relatively low ecliptic latitudes ($|b| < 30^\circ$). These criteria limit the Ulysses observations to those near perihelion and also exclude the Jupiter flybys

(see Figure 3). Note that filtering by rotation angle will not separate IPD from ISD because the interstellar flow direction was aligned with the heliocentric prograde motion (i.e., the dominant IPD direction) near perihelion (Strub et al., 2015). The selection criteria here yields dust observations at an average D_S of 1.36 AU. These observations occurred during four periods (see Figure 3) comprising a total of 0.76 years, which is the observing interval used for the Ulysses IPD flux quantities below.

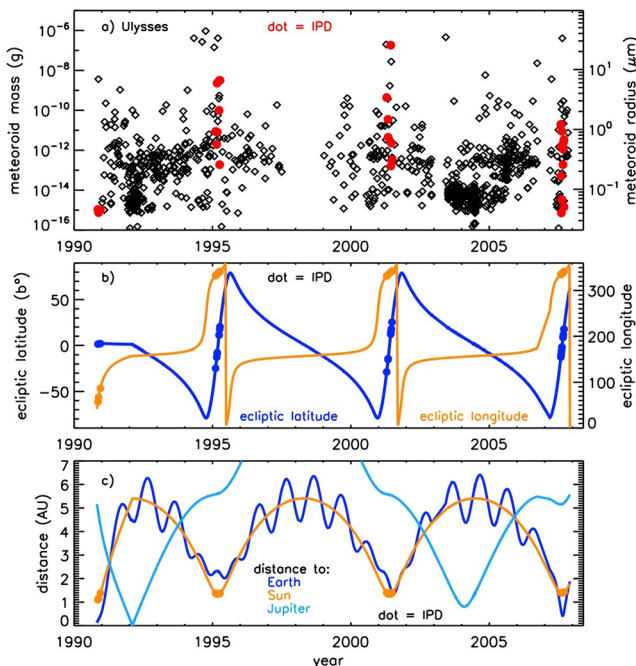


Figure 3. (a) Time series of individual Ulysses meteoroid detections in terms of the particle mass or radius (for $\rho = 2.65 \text{ g cm}^{-3}$). (b) The Ulysses ecliptic latitude and longitude. (c) Distance from the spacecraft to the Earth, Sun, and Jupiter. Observations used to identify a Interplanetary dust (IPD) in the near-Earth environment are indicated by dots ($D_S < 1.5 \text{ AU}$ and $|b| < 30^\circ$, see text for details).

5. Meteoric Mass Distributions

Interpreting the various measurements and relating them to each other requires an understanding of the meteoric mass distribution. The mass of meteoroids spans many orders of magnitude, with ISD ranging from 10^{-16} – 10^{-10} g ($r \approx 0.1$ – $2 \text{ } \mu\text{m}$, for $\rho = 2.65 \text{ g cm}^{-3}$) and IPD spanning roughly 10^{-15} to 10 g ($r \approx 0.1 \text{ } \mu\text{m}$ to 1 cm) (e.g., Krüger et al., 2019; Sterken et al., 2015). Visual meteors are roughly 10^{-2} to 10^3 g ($r \approx 0.1$ – 5 cm) but contribute little to the total meteoric mass influx at Earth, and larger bodies ($m > 1 \text{ kg}$) appear only on geologic time scales. Grün et al. (1985) (G85) described a meteoric mass distribution based on spacecraft in situ observations, lunar crater analysis, and photometric measurements of the Zodiacal light. The G85 expression yields the cumulative dust flux in free space, $n_C(m)$ ($\text{g m}^{-2} \text{ s}^{-1}$), for a given m (g) (i.e., the number of particles with mass $> m$),

$$n_C(m) = (2.2 \times 10^3 m^{0.306} + 15)^{-4.38} + 1.3 \times 10^{-9} (m + 10^{11} m^2 + 10^{27} m^4)^{-0.36} + 1.3 \times 10^{-16} (m + 106m^2)^{-0.85} \quad (1)$$

The number of particles with a given m , $n(m)$, is found from $n(m_i) = n_C(m_i) - n_C(m_{i+1})$. The number distribution is easily converted to a mass distribution, $f(m) = m n(m)$ (Grün et al., 1985).

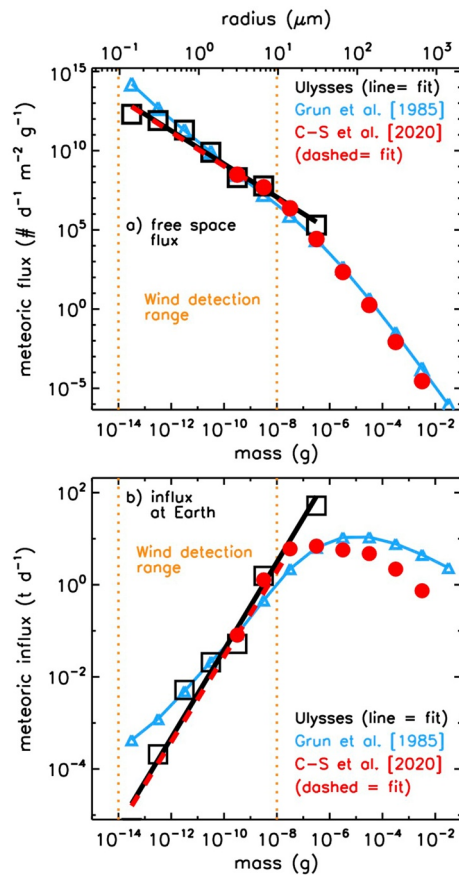


Figure 4. (a) Meteoric flux in free space versus particle mass (or radii for $\rho = 2.65 \text{ g cm}^{-3}$), as the daily number of meteoroids, per sample area, per mass interval (decade). Results are from Ulysses, Grün et al. (1985), and Carrillo-Sánchez et al. (2020). The Ulysses distribution is for observations at $D_S < 1.5 \text{ AU}$ and $|\text{bl}| < 30^\circ$, and a fit to values with $m > 10^{-14} \text{ g}$ is shown. The CS20 distribution was related to free space using Equation 3, and a fit to values for $m < 10^{-7} \text{ g}$ is shown. The mass range detected by Wind is indicated. (b) As in panel (a) except the distributions are in terms of the mass influx at Earth. The fit to Ulysses, $f_E(m) = 10^{8.1} m^{0.95} \text{ (t d}^{-1}, m \text{ in (g))}$, is similar to the fit to CS20 for $m < 10^{-7} \text{ g}$, $f_E(m) = 10^{7.7} m^{0.93} \text{ (t d}^{-1})$.

total meteoric influx at Earth, with $F_E = 37 \text{ t d}^{-1}$ for G85 and 28 t d^{-1} from CS20. Because Ulysses resolves the meteoroid mass, the individual observations can be added to give $F_E = 32 \text{ t d}^{-1}$. This is slightly more accurate than summing the histogram values, which assign the average mass to each interval. The reported Ulysses particle mass uncertainties are typically a factor of 5–10, and this error dominates the uncertainty in F_E . Even with the advantage of counting statistics (error reduction by $N^{-1/2}$) the Ulysses F_E uncertainty is large at 76 t d^{-1} . The above estimates are in good agreement with SOFIE observations which give $F_E = 25 \pm 7 \text{ t d}^{-1}$ on average (Hervig et al., 2021).

The meteoric mass and number distributions (Figure 4) were used to interpret the Wind observations, which do not resolve the mass of an impactor, but rather indicate the total flux of particles within the Wind mass detection range, $N_W = \sum_{m_1}^{m_2} n(m)$, with $m_1 = 10^{-14} \text{ g}$ and $m_2 = 10^{-8} \text{ g}$. N_W can be computed from the meteoric size distributions (e.g., Figure 4a), and used to provide and an estimate of the total influx at Earth from Wind,

$$F_E = N_W \sum_{m_1}^{m_2} f_E(m) / \sum_{m_1}^{m_2} n(m) = N_W C \quad (4)$$

The G85 expression and observations from Wind and Ulysses describe the meteoric flux in free space. Relating this to the flux into Earth's atmosphere requires consideration of Earth's gravity and surface area. The focusing effect of planetary gravity on meteoric dust was described by Drolshagen et al. (2017) as the enhancement factor

$$H_F = v^2 / (v^2 - v_{esc}^2) \quad (2)$$

where v is the dust velocity (far from Earth) and v_{esc} is the escape velocity (11.1 km s^{-1} for Earth) (see also Jones & Poole, 2007). The present study assumed a mean dust velocity of 17 km s^{-1} (e.g., Borin et al., 2017) giving $H_F = 1.74$, which is the value used below. The statistical uncertainty in H_F is $\sim 20\%$, for considering v in the range of $14\text{--}28 \text{ km s}^{-1}$. Earth's surface area is calculated at the typical meteor ablation altitude of 100 km ($S_E = 5.26 \times 10^{14} \text{ m}^2$). With these considerations the total meteoric influx at Earth, F_E , is given by

$$F_E = F H_F S_E \quad (3)$$

where F is the total flux in free space, $F = \sum f(m)$. Note that this expression is adaptable to the numeric or mass flux distributions as well (e.g., $f_E(m) = f(m) H_F S_E$, assuming constant v).

Ulysses observations in the near-Earth environment (see Section 4) were used to characterize the IPD mass distribution. The numeric flux distribution from Ulysses is compared to G85 in Figure 4a, along with results from Carrillo-Sánchez et al. (2020) (CS20) which describe $f(m)$ at Earth based on observations and models. The CS20 distribution (their Figure 1a) was related to free space here using Equation 3. The distributions from Ulysses and CS20 are in good agreement in the range where they overlap, and a log-linear fit to CS20 for $m < 10^{-7} \text{ g}$ is very close to the Ulysses values for smaller particles. The meteoric mass distributions from G85 and Ulysses were related to Earth using Equation 3, and are compared to the CS20 curve in Figure 4b. The distributions in terms of mass reveal some differences that are not apparent in the number distributions. In particular, both Ulysses and CS20 indicate lower influx than G85 for the smallest particles ($m < 10^{-10} \text{ g}$), while none of the distributions agree for the largest meteoroids ($m > 10^{-7} \text{ g}$). In the case of Ulysses, there are no observations of $m > 10^{-6} \text{ g}$, although the meteoric flux in the interval 10^{-7} to 10^{-6} g is ~ 4 times greater than for CS20 or G85. Note that the meteoric mass influx at Earth is dominated by particles in the range of 10^{-8} to 10^{-3} g . The sum of the distributions in Figure 4b gives the

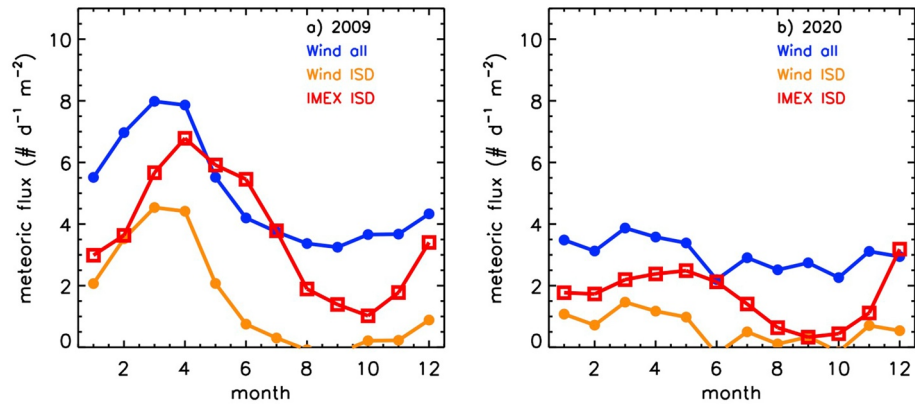


Figure 5. Meteoric flux as monthly means during (a) 2009 and (b) 2020. Results are for all observations from Wind, and Wind Interstellar dust (ISD) values which are the monthly mean minus the Wind Interplanetary dust (IPD) estimate (the average for September 22 ± 45 days). Results from the Interplanetary Meteoroid environment for EXploration (IMEX) model (Sterken et al., 2015) are near 1 AU for ISD with radii from 0.1 to 0.73 μm .

In this expression N_W is the Wind observation, and $C = \sum_{m_1}^{m_2} f_E(m) n(m)$ can be computed from a given modeled or measured mass distribution. Note that the summation of $f_E(m)$ is for the relevant range of IPD (roughly 10^{-9} to 10^{-2} g). For the mass distributions in Figure 4, $C = 2.1$ (t m^2) for G85 and $C = 11.3$ (t m^2) for CS20. One error component in C arise from the factor of 10 uncertainties in the Wind detection limits (m_1 and m_2) (Malaspina et al., 2014). This error component was estimated to be $\sim 29\%$, using the Ulysses mass distributions and perturbing m_1 and m_2 alternately by factors of 10 and 0.1. The total uncertainty in C from the G85 distribution is difficult to estimate, but it is at least 35% due to the combined errors in H_F (20%) and in m_1 and m_2 (29%). The uncertainty in C from CS20 is 70% due to errors in F_E , H_F , and m_1 and m_2 . The value for Ulysses was determined directly by summing the individual observations, giving $C = 9.9$ (t m^2). The uncertainty in C from Ulysses is close to a factor of ~ 3 , due to the uncertainty in F_E (discussed above) combined with the other terms. The value of C based on G85 is lower than from Ulysses or CS20 because the G85 curve indicates more dust at the smallest sizes. For comparison, the G85 distribution gives $N_W = 21.7$ $\text{d}^{-1} \text{m}^{-2}$, compared to 4.1 $\text{d}^{-1} \text{m}^{-2}$ from Ulysses and 2.4 $\text{d}^{-1} \text{m}^{-2}$ from CS20. While the small particles contribute little to the total mass, they contribute greatly to the total number of meteoroids (Figure 4). Equation 4 is used below with Wind observations to examine the IPD influx at Earth.

6. Decadal and Annual Variations in Meteoric Flux

Wind shows an annual cycle in meteoric flux, that varies in amplitude on a decadal time scale (e.g., Figure 2). The flux annual cycle is examined in greater detail in Figure 5, where the amplitude in 2009 is much larger than in 2020. This annual variation has been discussed by others (Kellogg et al., 2016; Malaspina et al., 2014; Wood et al., 2015; Zaslavsky et al., 2012), who concluded that higher flux near the Vernal equinox is associated with ISD. The reason is that Earth's ram direction is into the interstellar flow in March, and away from it in September (see also Malaspina et al., 2014). Because the Earth's orbital velocity (~ 30 km s^{-1}) is similar in magnitude to that of ISD (~ 26 km s^{-1}), the ISD flux detected by Wind approaches zero during September, when the velocities are nearly parallel (Figure 6). Given this pattern, Wind observations near the autumn equinox should represent mostly IPD, and an estimate of the IPD flux was determined from Wind as the mean of observations surrounding the autumn equinox (September 22 ± 45 days). It should be noted that the assumption of a constant ISD velocity here is a simplification (e.g., Sterken et al., 2012), and that faster and slower ISD can exist. It is thus possible that Wind measurements in September contain a few ISD, although a more detailed treatment of ISD velocities is beyond the scope of this paper. The ISD flux from Wind was subsequently obtained by

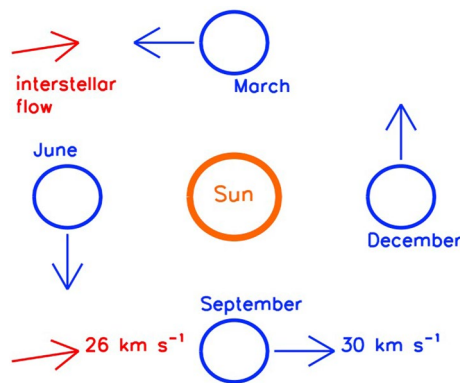


Figure 6. Diagram of Earth's position and velocity during the equinoxes and solstices (blue). The interstellar flow direction (259° ecliptic longitude) and velocity are indicated (red).

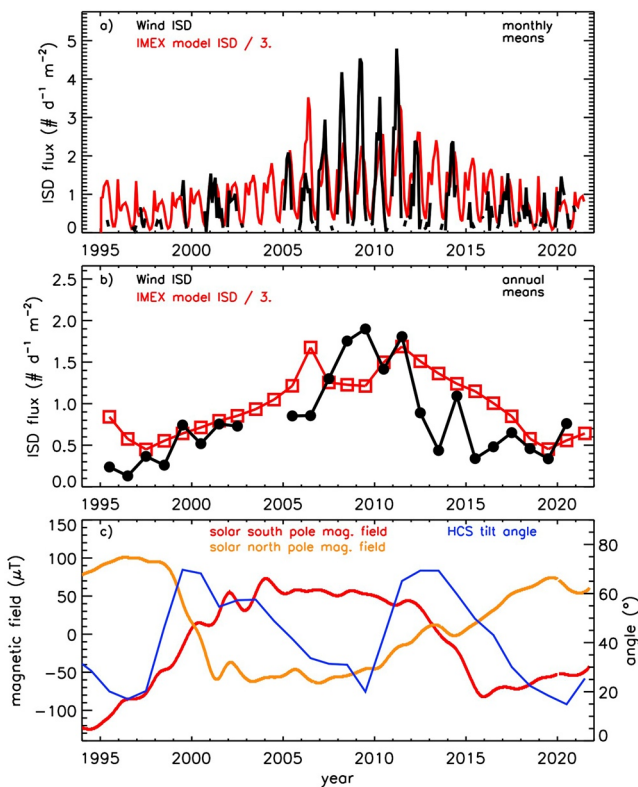


Figure 7. (a) Time series of interstellar dust flux as monthly means from Wind observations compared to Interplanetary Meteoroid environment for EXploration (IMEX) model simulations (divided by 3). (b) The Wind and IMEX interstellar dust flux as annual means. (c) Solar magnetic field strength at both poles and the heliospheric current sheet (HCS) tilt angle, from the Wilcox Solar Observatory.

subtracting the IPD flux from the monthly mean values during the rest of the year (Figure 5). The approach taken here for isolating IPD and ISD in Wind observations is similar to that used by Wood et al. (2015). The Wind ISD flux shows a strong annual variation, that is consistent with ISD flux simulations from the IMEX model (Krüger et al., 2019; Sterken et al., 2015). The IMEX results shown here are for the near Earth environment (1 AU), and ISD with radii from 0.1 to 0.73 μm . Note that both Wind and IMEX indicate a stronger spring ISD peak in 2009 than in 2020, which is explored below. The model peak occurs slightly later (April) than in Wind (March), which could be related to the assumed interstellar flow direction (259° ecliptic longitude) in IMEX. The model peak in ISD would occur at an earlier time if the interstellar flow was from a higher longitude (roughly 1 day per degree). Indeed, a slightly higher ecliptic longitude (274°) for ISD was considered by Sterken et al. (2014) in an interpretation of Stardust in situ ISD measurements. In additions, the analysis of Wind and Ulysses observations by Wood et al. (2015) also suggests that the interstellar flow comes from ecliptic longitudes greater than 259° .

Monthly mean ISD flux during 1995–2021 from Wind compare favorably to IMEX simulations (Figure 7a), with both indicating a stronger annual variation and greater overall ISD flux during 2004–2016. The trajectories of ISD in the solar system are controlled by solar gravity, solar radiation pressure, and magnetic field strength. Theory predicts that ISD flux should correlate to changes in the solar magnetic field (SMF), due to the Lorentz forces experienced by charged particles in motion (e.g., Landgraf et al., 2000; Sterken et al., 2015). The SMF varies with a 22-year periodicity (the Hale cycle, see Figure 7c), where the net effect on ISD is a focusing of particles in the inner heliosphere during solar south pole positive phases. Variations in the ISD flux are indeed coincident with changes in SMF, and linear regression to annual means gives correlation coefficients (p) of 0.74 for Wind and 0.67 for IMEX (Figure 7b). The heliospheric current sheet (HCS) tilt was also examined, which is a representation of the interplanetary magnetic field that exhibits an 11-year cycle (in phase with Lyman- α flux). The HCS is considered a factor in ISD trajectories (Sterken et al., 2015), although the Wind and IMEX ISD are only weakly correlated with the HCS tilt ($p = 0.1$ for Wind and 0.34 for IMEX). The good agreement between Wind and

IMEX confirms that Wind observations are dominated by ISD during spring. This agreement furthermore suggests that using Wind measurements near the autumn equinox provides a good approximation of IPD, which is important for characterizing the influx at Earth. Note that the Wind and IMEX results indicate an ISD influx at Earth (using Equation 3) of less than 0.01 t d^{-1} , which is insignificant compared to the IPD influx of $\sim 25 \text{ t d}^{-1}$.

Meteoric influx at Earth was estimated from the Wind IPD flux determined as above. The Wind F_E estimates use a constant (Equation 4) that is based on integrating the mass distributions from either Ulysses, G85, or CS20 (see Section 4). Wind F_E determined from the yearly IPD flux values are compared to SOFIE, Ulysses, and CS20 in Figure 8a. Wind F_E using C determined from G85 are much lower than when C from Ulysses or CS20, with the later providing Wind influx estimates that are in reasonable agreement with SOFIE, Ulysses, and CS20. Note that both Wind and SOFIE show similar year-to-year influx variations. The influx time series are compared to the SMF and HCS tilt angle in Figure 8b. Linear regression indicates a strong F_E —SMF correlation for both Wind ($p = 0.70$) and SOFIE ($p = 0.62$). The correlation with HCS tilt angle is weaker, however, with $p = 0.01$ for Wind and 0.42 for SOFIE. The Wind and SOFIE F_E time series are shown in Figure 8c with a fit to the results based on linear regression to the SMF. These results suggest that changes in the SMF can alter the flow of IPD in the inner heliosphere. This result is not anticipated, however, because IPD have small charge-to-mass ratios (Q/m), unlike ISD. While the IPD response to changing SMF would not be instantaneous, it is possible that a cumulative effect is realized after many orbits of the sun. This idea is supported somewhat by the apparent time delay in changing F_E with respect to SMF. Indeed, the highest F_E —SMF correlation is found for a time lag of 14 months, with $p = 0.76$ for Wind and 0.70 for SOFIE. The agreement between SOFIE and Wind concerning year-to-year and decadal changes in meteoric influx is encouraging, and furthermore suggests that variability in IPD appears in Earth's mesosphere.

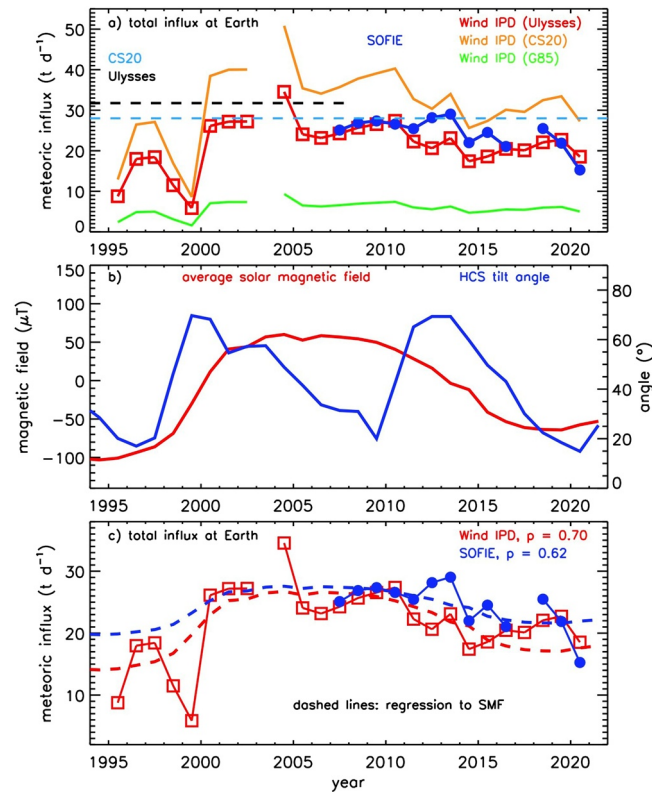


Figure 8. (a) Time series of total meteoric influx (F_E) at Earth. Wind results are shown for conversion factors based on the dust distribution from either Ulysses, Carrillo-Sánchez et al. (2020) (CS20), or Grün et al. (1985) (G85). Solar Occultation For Ice Experiment (SOFIE) results are the average for winter months near 67°N (Nov–Feb) and 67°S (June–September) (Hervig et al., 2021). The average influx based on Ulysses Interplanetary dust (IPD) observations during 1990–2007 is indicated ($|b| < 30^\circ$ and $D_S < 1.5$ AU). The CS20 F_E based on observations of iron and sodium in the mesosphere and cosmic spherules collected at South Pole is shown. (b) The North-South average solar polar magnetic field strength and HCS tilt angle, as annual means. (c) SOFIE and Wind F_E (C from Ulysses), with regressions to the average SMF time series and regression coefficients as listed.

The median F_E from Wind during 2007–2020 for C determined from the Ulysses, CS20, and G85 results are 22, 33, and 6 $t\ d^{-1}$, respectively, each with a standard deviation of $\sim 14\%$ during the time period. The median F_E based on the three Wind time series during 2007–2020 (i.e., Figure 8a) is 22 $t\ d^{-1}$, with a standard deviation of 11 $t\ d^{-1}$ (50%) which is due mostly to the spread in C . The total uncertainty in Wind F_E includes contributions from the error in H_F and uncertainties in the IPD flux measurements, and is closer to 13 $t\ d^{-1}$ (60%). Table 1 summarizes the meteoric influx estimates from this work and some recent publications.

Table 1
Total Meteoric Influx (Ablated + Surviving Material) at Earth From Different Sources

Source	Method	Meteoric influx ($t\ d^{-1}$)
Wind	Satellite in situ dust detection (2007–2020), <i>this work</i>	22 ± 13
Ulysses	Satellite in situ dust detection (1990–2007), <i>this work</i>	32 ± 76
SOFIE	Satellite remote measurements of meteoric smoke in the mesosphere (2007–2021) (Hervig et al., 2021)	25 ± 7
Lidar and cosmic spherules	Lidar measurements of Fe & Na in the mesosphere and cosmic spherules collected at South Pole (Carrillo-Sánchez et al., 2020)	28 ± 16
LDEF	Long Duration Exposure Facility (LDEF) satellite in situ dust measurements (1984–1990) (Borin et al., 2017)	15 ± 3
Lidar	Lidar measurements of Na in the mesosphere (Gardner et al., 2014)	60 ± 16

7. Summary

This work examined meteoric influx using in situ dust detection by the Wind and Ulysses spacecraft, and observations of meteoric smoke in the mesosphere by the SOFIE satellite instrument. Wind does not resolve the mass of the detected meteoroids, but rather reports the total number of particles with mass from 10^{-14} – 10^{-8} g. The Wind measurements were separated into the interstellar and interplanetary components. The Wind ISD measurements are in good agreement with simulations from the IMEX model, in terms of the both the annual and decadal flux variations. The decadal ISD variation is correlated to the 22-year solar magnetic cycle, as anticipated by theory and predicted by IMEX. The Wind IPD observations were related to the total meteoric influx at Earth using IPD mass distributions from Ulysses and previous publications. The resulting Wind influx estimates are in good agreement with SOFIE and Ulysses. The SOFIE and Wind time series show similar year-to-year and decadal variations in meteoric influx. The decadal influx variation exhibits an unanticipated correlation to the 22-year solar magnetic cycle. This relationship may be an artifact, or could indicate that changes in the SMF can alter the trajectories of interplanetary dust.

Data Availability Statement

SOFIE data are available online (sofie.gats-inc.com). WIND meteoric dust data are available online (cdaweb.gsfc.nasa.gov). Wilcox Solar Observatory data are available online (<http://wso.stanford.edu>). Ulysses dust observations are available online (cdaweb.gsfc.nasa.gov).

References

- Andersson, L., Weber, T. D., Malaspina, D., Cray, F., Ergun, R. E., Delory, G. T., et al. (2015). Dust observations at orbital altitudes surrounding Mars. *Science*, *350*(6261), 398. <https://doi.org/10.1126/science.aad0398>
- Bardeen, C. G., Toon, O. B., Jensen, E. J., Marsh, D. R., & Harvey, V. L. (2008). Numerical simulations of the three-dimensional distribution of meteoric dust in the mesosphere and upper stratosphere. *Journal of Geophysical Research*, *113*(D17), D17202. <https://doi.org/10.1029/2007JD009515>
- Borin, P., Cremonese, G., Marzari, F., & Lucchetti, A. (2017). Asteroidal and cometary dust flux in the inner solar system. *Astronomy & Astrophysics*, *605*, A94. <https://doi.org/10.1051/0004-6361/201730617>
- Bougeret, J., Kaiser, M. L., Kellogg, P. J., Manning, R., Goetz, K., Monson, S. J., et al. (1995). Waves: The radio and plasma wave investigation on the wind spacecraft. *Space Science Reviews*, *71*(1–4), 231–263. <https://doi.org/10.1007/BF00751331>
- Carrillo-Sánchez, J. D., Gómez-Martín, J. C., Bones, D. L., Nesvorný, D., Pokorný, P., Benna, M., et al. (2020). Cosmic dust fluxes in the atmospheres of Earth, Mars, and Venus. *Icarus*, *335*, 113395. <https://doi.org/10.1016/j.icarus.2019.113395>
- Drolshagen, G., Koschny, D., Drolshagen, S., Kretschmer, J., & Poppe, B. (2017). Mass accumulation of Earth from interplanetary dust, meteoroids, asteroids and comets. *Planetary and Space Science*, *143*, 21–27. <https://doi.org/10.1016/j.pss.2016.12.010>
- Fentzke, J. T., Janches, D., & Sparks, J. J. (2009). Latitudinal and seasonal variability of the micrometeor input function: A study using model predictions and observations from Arecibo and PFSR. *Journal of Atmospheric and Solar-Terrestrial Physics*, *71*(6–7), 653–661. <https://doi.org/10.1016/j.jastp.2008.07.015>
- Gardner, C. S., Alan, Z., Liu, D. R., Wuhu, F., & Plane, J. M. C. (2014). Inferring the global cosmic dust influx to the Earth's atmosphere from Lidar observations of the vertical flux of mesospheric Na. *Journal of Geophysical Research: Space Physics*, *119*(9), 7870–7879. <https://doi.org/10.1002/2014JA020383>
- Grün, E., Fechtig, H., Kissel, J., Linkert, D., Maas, D., McDonnell, J. A. M., et al. (1992). The Ulysses dust experiment. *Astronomy & Astrophysics Supplement Series*, *92*, 411–423.
- Grün, E., Zook, H. A., Fechtig, H., & Giese, R. H. (1985). Collisional balance of the meteoritic complex. *Icarus*, *62*(2), 244–272. [https://doi.org/10.1016/0019-1035\(85\)90121-6](https://doi.org/10.1016/0019-1035(85)90121-6)
- Gurnett, D. A., Grun, E., Gallagher, D., Kurth, W. S., & Scarf, F. L. (1983). Micron-sized particles detected near Saturn by the Voyager plasma wave instrument. *Icarus*, *53*(2), 236–254. [https://doi.org/10.1016/0019-1035\(83\)90145-8](https://doi.org/10.1016/0019-1035(83)90145-8)
- Hervig, M. E., Brooke, J. S. A., Feng, W., Bardeen, C. G., & Plane, J. M. C. (2017). Constraints on meteoric smoke composition and meteoric influx using SOFIE observations with models. *Journal of Geophysical Research: Atmospheres*, *122*(24), 13495–13505. <https://doi.org/10.1002/2017JD027657>
- Hervig, M. E., Deaver, L. E., Bardeen, C. G., Russell, J. M., Bailey, S. M., & Gordley, L. L. (2012). The content and composition of meteoric smoke in mesospheric ice particles from SOFIE observations. *Journal of Atmospheric and Solar-Terrestrial Physics*, *84*–85, 1–6. <https://doi.org/10.1016/j.jastp.2012.04.005>
- Hervig, M. E., Gordley, L. L., Deaver, L. E., Siskind, D. E., Stevens, M. H., Russell, J. M., III, et al. (2009). First satellite observations of meteoric smoke in the middle atmosphere. *Geophysical Research Letters*, *36*(18), L18805. <https://doi.org/10.1029/2009GL039737>
- Hervig, M. E., Plane, J. M. C., Siskind, D. E., Feng, W., Bardeen, C. G., & Bailey, S. M. (2021). New global meteoric smoke observations from SOFIE: Insight regarding chemical composition, meteoric influx, and hemispheric asymmetry. *Journal of Geophysical Research: Atmospheres*, *126*(13), e2021JD035007. <https://doi.org/10.1029/2021JD035007>
- Janches, D., Palo, S. E., Lau, E. M., Avery, S. K., Avery, J. P., de la Peña, S., & Makarov, N. A. (2004). Diurnal and seasonal variability of the meteoric flux at the South Pole measured with radars. *Geophysical Research Letters*, *31*(20), L20807. <https://doi.org/10.1029/2004GL021104>
- Jones, J., & Poole, M. G. (2007). Gravitational focusing and shielding of meteoroid streams. *Monthly Notices of the Royal Astronomical Society*, *375*(3), 925–930. <https://doi.org/10.1111/j.1365-2966.2006.11349>
- Kellogg, P. J., Goetz, K., & Monson, S. J. (2016). Dust impact signals on the wind spacecraft. *Journal of Geophysical Research: Space Physics*, *121*(2), 966–991. <https://doi.org/10.1002/2015JA021124>

Acknowledgments

This work was funded in part by the AIM mission through NASA contract NAS5-03132. V. J. Sterken received funding from the European Union's Horizon 2020 research and innovation program under Grant agreement N851544. L. B. Wilson was partially supported by Wind MO&DA funds.

- Krüger, H., Altobelli, N., Anweiler, B., Dermott, S. F., Dikarev, V., Graps, A. L., et al. (2006). Five years of Ulysses dust data: 2000–2004. *Planetary and Space Science*, 54(9–10), 932–956. <https://doi.org/10.1016/j.pss.2006.04.015>
- Krüger, H., Strub, P., Altobelli, N., Sterken, V. J., Srama, R., & Grün, E. (2019). Interstellar dust in the solar system: Model versus in situ spacecraft data. *Astronomy & Astrophysics*, 626, A37. <https://doi.org/10.1051/0004-6361/201834316>
- Krüger, H., Strub, P., Grün, E., & Sterken, V. J. (2015). Sixteen years of Ulysses interstellar dust measurements in the solar system. I. Mass distribution and gas-to-dust mass ratio. *The Astrophysical Journal*, 812(2), 139. <https://doi.org/10.1088/0004-637X/812/2/139>
- Landgraf, M., Baggaley, W. J., Grün, E., Krüger, H., & Linkert, G. (2000). Aspects of the mass distribution of interstellar dust grains in the solar system from in situ measurements. *Journal of Geophysical Research*, 105(A5), 10343–10352. <https://doi.org/10.1029/1999ja900359>
- Malaspina, D. M., Horanyi, M., Zaslavsky, A., Goetz, K., Wilson, L. B., III., & Kersten, K. (2014). Interplanetary and interstellar dust observed by the Wind/WAVES electric field instrument. *Geophysical Research Letters*, 41(2), 266–272. <https://doi.org/10.1002/2013GL058786>
- Malaspina, D. M., & Wilson, L. B., III. (2016). A database of interplanetary and interstellar dust detected by the Wind spacecraft. *Journal of Geophysical Research: Space Physics*, 121(10), 9369–9377. <https://doi.org/10.1002/2016JA023209>
- Mann, I., Nouzák, L., Vaverka, J., Antonsen, T., Fredriksen, Å., Issautier, K., et al. (2019). Dust observations with antenna measurements and its prospects for observations with Parker Solar Probe and Solar Orbiter. *Annals of Geophysics*, 37, 1121–1140. <https://doi.org/10.5194/angeo-2019-94>
- Megner, L., Siskind, D. E., Rapp, M., & Gumbel, J. (2008). Global and temporal distribution of meteoric smoke; a 2D simulation study. *Journal of Geophysical Research*, 113(D3), D03202. <https://doi.org/10.1029/2007JD009054>
- Meyer-Vernet, N., Moncuquet, M., Issautier, K., & Lecacheux, A. (2014). The importance of monopole antennas for dust observations: Why Wind/WAVES does not detect nanodust. *Geophysical Research Letters*, 41(8), 2716–2720. <https://doi.org/10.1002/2014GL059988>
- Plane, J. M. C. (2012). Cosmic dust in the Earth's atmosphere. *Chemical Society Reviews*, 41(19), 6507–6518. <https://doi.org/10.1039/c2cs35132c>
- Reid, I. M., Holdsworth, D. A., Morris, R. J., Murphy, D. J., & Vincent, R. A. (2006). Meteor observations using the Davis mesosphere stratosphere-troposphere radar. *Journal of Geophysical Research*, 111(A5), A05305. <https://doi.org/10.1029/2005JA011443>
- Rudraswami, N. G., Ppandey, M., Genge, M. J., Fernandes, D., & Brownlee, D. (2021). Extraterrestrial dust as a source of bioavailable iron contributing to the ocean for driving primary productivity. *Meteoritics & Planetary Sciences*, 56(Nr 12), 2175–2190. <https://doi.org/10.1111/maps.13764>
- Russell, J. M., III., Bailey, S. M., Gordley, L. L., Rusch, D. W., Horanyi, M., Hervig, M. E., et al. (2009). Aeronomy of Ice in the mesosphere (AIM): Overview and early science results. *Journal of Atmospheric and Solar-Terrestrial Physics*, 71(3–4), 289–299. <https://doi.org/10.1016/j.jastp.2008.08.011>
- Shen, M. M., Sternovsky, Z., Garzelli, A., & Malaspina, D. M. (2021). Electrostatic model for antenna Signal generation from dust Impacts. *Journal of Geophysical Research: Space Physics*, 126(9), e29645. <https://doi.org/10.1029/2021JA029645>
- Singer, W., von Zahn, U., & Weiß, J. (2004). Diurnal and annual variations of meteor rates at the Arctic circle. *Atmospheric Chemistry and Physics*, 4(5), 1355–1333. <https://doi.org/10.5194/acp-4-1355-2004>
- Soja, R. H., Grün, E., Strub, P., Sommer, M., Millinger, M., Vaubaillon, J., et al. (2019). IMEM2: A meteoroid environment model for the inner solar system. *Astronomy & Astrophysics*, 628, A109. <https://doi.org/10.1051/0004-6361/201834892>
- Sterken, V. J., Altobelli, N., Kempf, S., Schwehm, G., Srama, R., & Grün, E. (2012). The flow of interstellar dust into the solar system. *Astronomy & Astrophysics*, 538, A102. <https://doi.org/10.1051/0004-6361/201117119>
- Sterken, V. J., Strub, P., Krüger, H., von Steiger, R., & Frisch, P. (2015). Sixteen years of Ulysses interstellar dust measurements in the solar system. III. Simulations and data unveil new insights into local interstellar dust. *The Astrophysical Journal*, 812(2), 141. <https://doi.org/10.1088/0004-637X/812/2/141>
- Sterken, V. J., Westphal, A., Altobelli, N., Grün, E., Hillier, J. K., Postberg, F., et al. (2014). Stardust Interstellar Preliminary examination X: Interstellar dust simulations for the Stardust mission. *Meteoritics & Planetary Sciences*, 49(9), 1690–1697. <https://doi.org/10.1111/maps.12219>
- Sterken, V. J., Westphal, A. J., Altobelli, N., Malaspina, D., & Postberg, F. (2019). Interstellar dust in the solar system. *Space Science Reviews*, 215(7), 43. <https://doi.org/10.1007/s11214-019-0607-9>
- Strub, P., Krüger, H., & Sterken, V. J. (2015). Sixteen Years of Ulysses Interstellar Dust Measurements in the Solar System: II. Fluctuations in the Dust Flow from the Data. *Astrophysical Journal*, 812. <https://doi.org/10.1088/0004-637X/812/2/140>
- Strub, P., Sterken, V. J., Soja, R., Krüger, H., Grün, E., & Srama, R. (2019). Heliospheric modulation of the ISD flow onto Earth. *Astronomy & Astrophysics*, 621, A54. <https://doi.org/10.1051/0004-6361/201832644>
- Wilson, L. B., Brosius, A. L., Gopalswamy, N., Nieves-Chinchilla, T., Szabo, A., Hurley, K., et al. (2021). A quarter century of wind spacecraft discoveries. *Reviews of Geophysics*, 59(2), e2020RG000714. <https://doi.org/10.1029/2020RG000714>
- Wood, S. R., Malaspina, D. M., Andersson, L., & Horanyi, M. (2015). Hypervelocity dust impacts on the wind spacecraft: Correlations between Ulysses and wind inter-stellar dust detections. *Journal of Geophysical Research: Space Physics*, 120(9), 7121–7129. <https://doi.org/10.1002/2015JA021463>
- Zaslavsky, A., Meyer-Vernet, N., Mann, I., Czechowski, A., Issautier, K., Le Chat, G., et al. (2012). Interplanetary dust detection by radio antennas: Mass calibration and fluxes measured by STEREO/WAVES. *Journal of Geophysical Research*, 117(A5), A05102. <https://doi.org/10.1029/2011JA017480>